

## Chapter 20

# Linear Take-Off and Landing of a Rigid Aircraft for Airborne Wind Energy Extraction

Lorenzo Fagiano, Eric Nguyen Van and Stephan Schnez

**Abstract** An overview of recent results on the take-off and landing phases of airborne wind energy systems with a rigid aircraft is given. The considered take-off approach employs a linear motion system installed on the ground to accelerate the aircraft to take-off speed and on-board propellers to sustain the climb up to operational altitude. Theoretical analyses are employed to estimate the power, additional on-board mass and land occupation required to realize such a take-off strategy. A realistic dynamical model of the tethered aircraft is then employed, together with a decentralized control approach, to simulate the take-off maneuver, followed by a low-tension flight and a landing maneuver back on the linear motion system. The consequences of different wing loadings for this approach are discussed as well. The simulation results indicate that the take-off and landing can also be accomplished in turbulent wind conditions with good accuracy when the wing loading is relatively small. On the other hand, with larger wing loading values the performance is worse. Possible ways to improve the approach and further research directions are finally pointed out.

## 20.1 Introduction

The take-off and landing phases of airborne wind energy systems employing rigid aircraft and pumping cycles are among the aspects that received relatively little attention in the last decade. In fact, this functionality has been demonstrated, at least on a small-scale, in systems with on-board generation [16, 17] and in systems based on pumping cycles and flexible wings [9], using a rather compact ground area. For AWE systems with rigid wings and ground-level electric generators, there is also evidence of autonomous take-off [1], however by using a winch launch that requires

---

Lorenzo Fagiano · Eric Nguyen Van · Stephan Schnez (✉)  
ABB Switzerland Ltd, Corporate Research, Segelhofstrasse 1K, 5405 Baden-Dättwil, Switzerland  
e-mail: [stephan.schnez@ch.abb.com](mailto:stephan.schnez@ch.abb.com), [eric.nguyenvan@protonmail.ch](mailto:eric.nguyenvan@protonmail.ch), [lorenzo.fagiano@polimi.it](mailto:lorenzo.fagiano@polimi.it)

a significant space in all directions in order to adapt to the prevalent wind direction during take-off. Regarding the landing phase, to the best of the authors' knowledge this has been demonstrated and documented only by detaching the tether from the aircraft, which can be dangerous and impractical due to the absence of control on the tether behavior after detachment, and the need to re-attach it to the aircraft for the subsequent take-off.

So far, this issue has been addressed to a limited extent within the scientific community, where only the take-off phase has been partially studied. In Ref. [10], a rotational take-off is considered and simulated with a focus on the control and optimization aspects. Reference [2] gives an analysis of several take-off strategies, considering different performance criteria. There, three alternatives are deemed the most promising: buoyant systems, linear ground acceleration plus on-board propeller, and rotational take-off. Then, the rotational take-off is examined in more detail by means of numerical simulations.

At ABB Corporate Research, we recently started to investigate this problem via theoretical, numerical and experimental research. In a first contribution [7], we provide a theoretical study of three possible take-off approaches, aimed to assess and compare their technical and economic viability. Out of this study, we conclude that the most promising approach for the considered type of AWE system is to combine a linear acceleration phase on the ground, using a ground-level linear motion system, with on-board propellers, to sustain the climb of the aircraft to operational altitude. In the AWE community, the company Ampyx Power is currently exploring such an approach for their system [11]. In a second contribution [14], we then study the modeling and control design aspects of this approach, including the landing phase without detaching the tether and aiming to touch ground back on the linear motion system used for the take-off. In the same reference we provide realistic numerical simulations that indicate that a satisfactory landing accuracy can be obtained, even in the presence of wind turbulence, with an aircraft with low wing loading.

In this chapter, we provide an overview of the mentioned findings, and we exploit the developed tools to further comment on the effects of the wing loading on both the take-off and landing phases. In particular, we show how the additional power (both on the ground and on board), the additional on-board mass, and the ground area required for take-off change with the wing loading, and how the flight pattern and wind conditions that can be managed successfully during landing are affected by this parameter.

The chapter is structured as follows. Section 20.2 provides a brief description of the considered take-off and landing strategy. Section 20.3 summarizes the main findings pertaining to the theoretical analysis of the approach, as well as new considerations on the effects of the wing loading. Section 20.4 presents the results concerning modeling and control design of the system. Section 20.5 describes the obtained simulation results. Finally, Sect. 20.6 provides conclusions and further steps in this research. The preliminary content of the present chapter has been presented at the Airborne Wind Energy Conference 2015 [8].

## 20.2 Linear Take-Off and Landing: System Description and Operation

In Ref. [7], we analyzed four different launching procedures which are conceivable for an AWE concept based on a rigid wing and ground-based electric generation: a vertical take-off with vertical-axis propellers, a rotational take-off on a carousel-like structure, a linear take-off with small on-board propellers, and a standard winch launch. Based on qualitative and quantitative performance criteria, we concluded that the linear take-off is the most appealing approach. Here, we will summarize the most important results from Ref. [7] for the linear take-off and investigate the influence of the wing loading more deeply.

### 20.2.1 System Description

The system we consider is composed of a ground station equipped with a winch, storing a tether connected to a rigid aircraft, see Fig. 20.1 for a sketch and Fig. 20.2 for a picture of our small-scale experimental setup. Details of the prototype are reported in Ref. [4]. Two electric machines are installed on the ground station: The first one controls the winch in order to achieve, during power production, a repetitive cycle of reeling-out under high load, hence converting the mechanical power into electrical, and of reeling-in under low load, spending a small fraction of the energy to start a new production phase. The second machine controls the movement of a linear motion system composed of a slide on rails. In particular, in the approach we consider here, the slide can be pulled both forward and backwards by two tethers,

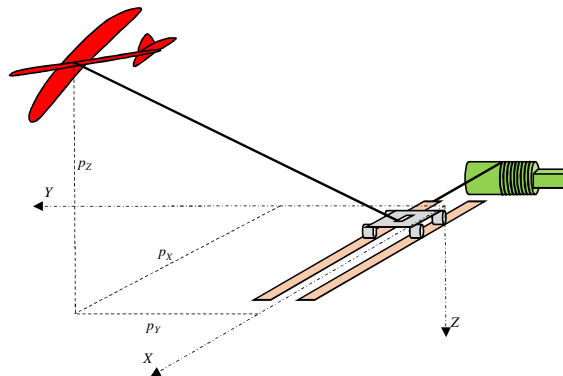


**Fig. 20.1** Sketch of the considered system together with the  $(X, Y, Z)$  inertial frame and the position  $[p_x, p_y, p_z]^T$  of the aircraft. The electrical motor controlling the slide position is not depicted

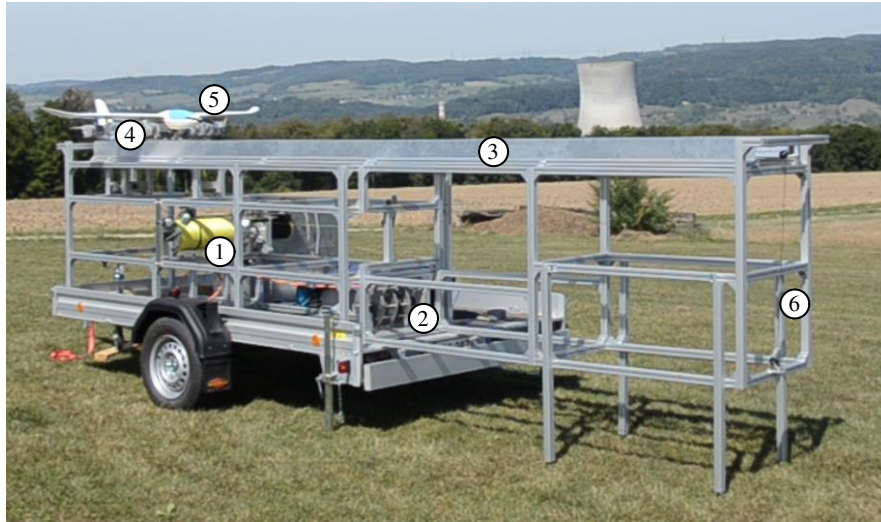


**Fig. 20.2** Photo of the small-scale prototype built at ABB Corporate Research. The numbers in the picture indicate: ① the winch, ② the motor that moves the slide via a pair of additional tethers, ③ the rails, ④ the slide, ⑤ the rigid aircraft, ⑥ the aluminum frame. The rails are 4.5 m long and about 0.5 m wide. The employed aircraft is a commercial model made of Styrofoam, with 1.85-m-wingspan, a mass of about 1 kg, and a propeller connected to a 300 W DC motor. It has been modified to host a tether attach/detach mechanism, an inertial measurement unit and an autopilot. 200 meters of Dyneema<sup>®</sup> tether with 0.002 m diameter are coiled on the winch. The motor connected to the winch and the one connected to the slide are ABB permanent-magnet, three-phase motors with 2 kW of rated power and 13 Nm of rated torque, controlled by two ABB MicroFlex<sup>®</sup> drives

which are coiled around a drum (“slide drum”) attached to the second electric motor, see Fig. 20.2. A series of pulleys redirects the tether from the winch to the slide and then to the aircraft. The position and speed of both electric machines are measured via encoders and hall-effect sensors. The position of the ground station is determined via global positioning system (GPS). The tether tension is estimated by measuring the compression of a tether tensioning system installed in the ground station. All these measurements can be used for feedback control of the ground station. The available manipulated variables on the ground are the torques of the two electric machines. The tether is made of ultra-high-molecular-weight polyethylene.

We consider a rigid aircraft with on-board electric propellers. The aircraft’s attitude, absolute position, angular rates and linear velocity vector are measured with an inertial measurement unit (IMU) and a GPS. The incoming airspeed along the longitudinal body axis is also measured using an air speed sensor. The available control surfaces are the ailerons (for roll control), elevator (for pitch control), rudder (for yaw control), and flaps (to increase lift and drag during take-off and landing). Together with the propellers’ thrust, these form the five manipulated variables available to influence the aircraft’s motion. In our experimental setup (see Fig. 20.2) the air-

craft is a commercially available model made of foam, which is inexpensive, easy to modify and resilient to impacts.

### 20.2.2 System Operation

We can divide the desired system operation in three phases:

**Take-off** The aircraft is initially attached to the slide. The slide is accelerated to take-off speed and decelerated down to rest within the length of the rails. The aircraft starts its on-board propulsion during the acceleration and detaches from the slide when the peak speed has been reached.

**Flight** Since power generation is not our objective, transition from normal flight to pumping cycles is not considered here. Instead, the aim is to control the flight at relatively low speed, notwithstanding the perturbation induced by the tether and by wind turbulence, and to prepare for the landing procedure. To this end, a roughly rectangular path is executed before approaching the ground station for landing.

**Landing** The landing strategy we consider consists in reeling in the tether to guide the aircraft to the rails. When it is close enough to the ground station, the winch is stopped and the slide starts to accelerate, hence reeling-in the remaining part of the tether and engaging again with the aircraft. Finally, the slide is slowed down and the tether is used to keep the aircraft on it during the braking.

In the considered concept, the take-off is the most energy-intensive phase and determines the system requirements in terms of power (both on the ground and on board), additional on-board mass, and ground area. On the other hand, the landing phase requires accurate and fast control, but it does not consume additional energy in principle. Rather, the kinetic and potential energy of the aircraft have to be dissipated in a controlled way.

Thus, in the following we first focus our attention on the take-off phase and we analyze its requirements and its impact on the design of the whole AWE generator (Sect. 20.3), and then we consider the control problem for the whole cycle of take-off, flight and landing (Sect. 20.4).

## 20.3 Power, Mass and Ground Area Required for the Take-Off Phase

The considered AWE system generates energy by means of a pumping operating principle composed of the power-generation (or traction) phase, the retraction phase, and the transition phases linking them [6]. During the traction phase, the on-board control system steers the aircraft into figure-of-eight patterns under crosswind conditions. The generated aerodynamic forces exert a large traction load on the tether,

which is reeled out from the winch. The winch drives an electric machine and thus generates electricity. Under perfect crosswind conditions (i.e. the tether is parallel to the incoming wind) and a reel-out speed equal to one third of the wind speed, the maximum mechanical power is generated [12]:

$$P_m^* = \frac{2}{27} \rho A \frac{C_L^3}{C_{D,eq}^2} v_w^3, \quad (20.1)$$

where  $\rho$  is the air density,  $A$  the effective area of the aircraft,  $C_L$  and  $C_{D,eq}$  the aerodynamic lift and drag (including tether drag) coefficients, and  $v_w$  the absolute wind speed.

For the sake of estimating the generated power, the mass of the airborne components is irrelevant in a first approximation, since the weight and apparent forces of the aircraft and of the tether are significantly smaller than the force acting on the tether during the traction phase. On the other hand, this parameter clearly plays a crucial role when discussing take-off approaches. In order to evaluate a given take-off technique on a quantitative basis, the total mass of the aircraft  $m$  has to be linked to the system's capability in terms of force and power. Such a link is given by the so-called wing loading  $w_l$ , i.e. the ratio between  $m$  and  $A$ :

$$m = w_l A. \quad (20.2)$$

The total mass of the aircraft is then the sum of  $m$  and of the additional mass  $\Delta m$  required for the take-off capability, as further discussed below.

### 20.3.1 Acceleration Phase on the Ground

The acceleration phase on the ground lasts until the take-off speed  $v^*$  is reached:

$$v^* = \sqrt{\frac{2(m + \Delta m)g}{\rho A C_L}}, \quad (20.3)$$

computed by setting  $F_L = (m + \Delta m)g$  and using  $F_L = \frac{1}{2}\rho A C_L v^{*2}$ . Assuming that this speed shall be reached after a horizontal acceleration distance  $L$ , the required acceleration is  $a = v^{*2}/(2L)$ . The corresponding required force is then  $F_g = (m + \Delta m)a$ . The other forces acting at take-off are significantly smaller, but not negligible, namely the drag force  $F_D = \frac{1}{2}\rho C_{D,eq} A v^{*2}$  and the viscous resistance  $F_v = c_v v^*$ , where  $c_v$  is the viscous friction coefficient of the system employed for the linear acceleration. Hence, the required maximal power on the ground,  $\bar{P}_g$ , is

$$\begin{aligned} \bar{P}_g &= v^* (F_g + F_D + F_v) \\ &= \frac{\sqrt{2}(m + \Delta m)^{5/2} g^{3/2}}{L(\rho A C_L)^{3/2}} + \frac{C_{D,eq}(2g(m + \Delta m))^{3/2}}{\sqrt{\rho A C_L^3}} + \frac{2g(m + \Delta m)c_v}{\rho A C_L}. \end{aligned} \quad (20.4)$$

As we comment later on, the additional mass  $\Delta m$  results to be proportional to the mass  $m$  of the aircraft without considering the take-off equipment. Hence, Eqs. (20.3) and (20.4) reveal that, for given wing loading and aerodynamic coefficients, the take-off speed is independent of the wing's size and that, for a fixed travel distance, the peak required ground power is proportional to the effective area in a first approximation. Moreover, Eq. (20.4) clearly shows that, if the take-off distance  $L$  is small, e.g. of the same order of magnitude of the aircraft wingspan, the inertia of the plane (and of the linear motion system) is the dominating term in the power requirement on the ground, since  $C_{D,eq}$  and  $c_v$  are small.

As regards the land occupation  $A_g$ , we choose to fix the acceleration distance  $L$  on the rails, such that it is independent from the wing size, and we assume that the system shall be able to adapt to the widest possible range of prevalent wind conditions, i.e. the linear acceleration phase can be carried out in all directions. At the same time, the area spanned by the wings throughout the ground launching phase is considered to be occupied by the system. Thus, we obtain

$$A_g \simeq \frac{\pi L^2}{4} + \frac{\pi d^2}{4}, \quad (20.5)$$

where  $d$  is the wingspan of the aircraft.

### 20.3.2 Powering the Plane During the Ascend

We analyze the climbing phase assuming the worst conditions possible, i.e. with zero prevalent wind speed, which yields the required peak on-board power. It turns out that the required propeller thrust is approximately equal to

$$F_T \approx (m + \Delta m)g \left( \frac{C_{D,eq}}{C_L} + c_r \right), \quad (20.6)$$

where  $c_r$  denotes the ratio of the vertical speed  $v_c$  and the horizontal (forward) speed  $v_{\text{fwd}}$  (see Fig. 20.3). We refer to Ref. [7] for a detailed derivation. The required on-board power is then (see [7])

$$\bar{P}_{ob} = \frac{F_T}{\eta} \left( \sqrt{\frac{F_T}{2\rho A_{\text{prop}}} + \frac{v_{\text{fwd}}^2}{4}} + \frac{1}{2}v_{\text{fwd}} \right), \quad (20.7)$$

Here, we consider two propellers with a total area  $A_{\text{prop}}$ , each having a diameter of half the chord (where the chord length is the distance from the leading to the trailing edge of the wing), with horizontal axes, and with an efficiency of  $\eta$ .

Finally, as regards the additional on-board mass  $\Delta m$ , this is mainly determined by the on-board batteries and the electric motors that drive the propellers. The required battery mass is calculated from the energy density of lithium-polymer batteries  $E_{\text{batt}}$  and the required power  $P_{ob}$ , target altitude  $h$  and climb speed  $v_c$  (i.e. the climb du-

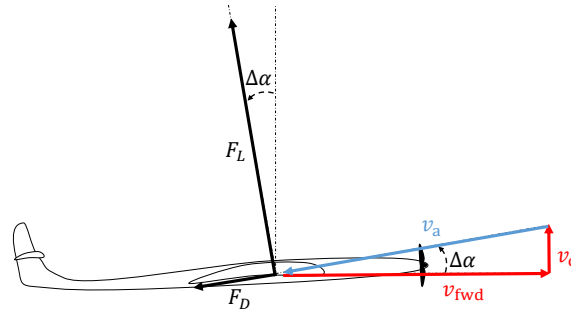


**Fig. 20.3** Schematic representation of an airplane with horizontal speed of  $v_{\text{fwd}}$  (assuming no wind) and a vertical speed of  $v_c$ . The lift force has a component opposite to the thrust and the drag force has a component which adds to the gravitational pull

ration is  $h/v_c$ ). The power density of an electric motor is indicated by  $E_{\text{mot}}$ . The resulting equation for the additional on-board mass is:

$$\Delta m = P_{ob} \left( \frac{h}{v_c E_{\text{batt}}} + \frac{1}{E_{\text{mot}}} \right). \quad (20.8)$$

We solve Eqs. (20.6) to (20.8) to compute the required on-board power, accounting also for the additional mass.

### 20.3.3 Results and Discussion

We evaluate expressions given by Eqs. (20.1) to (20.8) for the input parameters given in Table 20.1 for three different wing sizes, namely 5, 10 and 20 m wingspan. The results are reported in bold numbers in the Table. It turns out that the required power values—be it on the ground or on board—are small compared to the generated (mechanical) power: the required on-ground power is about 11% of the peak mechanical power (at a wind speed of 15 m/s and with take-off travel  $L = 12$  m); the on-board power only 3%. The rather small power which is required on board results in a weight increase of 5%.

Some aspects should be pointed out:

- The required power on the ground could, in principle, be provided by the electric machine connected to the winch: one could envision a solution where this machine is also employed in the initial phase of the take-off, e.g. by means of a clutch to (dis-) engage a linear motion system to accelerate the aircraft. In our prototype, we use an additional electric motor for simplicity.
- The required ground occupation is dominated by the wing size when scaling up. Hence, it turns out to be quite favorable.

Parameter	Aircraft 1	Aircraft 2	Aircraft 3
Wing span $d$ (m)	5	10	20
Aspect ratio $\mathcal{R}$		10	
Chord $d/\mathcal{R}$ (m)	0.5	1	2
Wing area $A$ (m <sup>2</sup> )	2.5	10	40
Wing loading $w_l = m/A$ (kg/m <sup>2</sup> )		15	
Mass $m$	37.5	150	600
Lift coefficient $C_L$		1	
Drag coefficient $C_{D,eq}$		0.1	
Desired vertical velocity $v_c$ (m/s)		1	
Propeller efficiency $\eta$		0.7	
Peak mech. power $P_m^*$ at $W = 15$ m/s (kW)	75	300	1200
Ground travel distance $L$ (m)		12	
Target height $h$ (m)		100	
Viscous friction coefficient $c_v$ (kg/s)	0.1	0.3	1
Take-off speed $v^*$ (m/s)		<b>15.7</b>	
Propeller's diameter $d/(2\mathcal{R})$ (m)	0.25	0.5	1
Peak additional ground power $\bar{P}_g$ (kW)	<b>8</b>	<b>31</b>	<b>124</b>
Peak additional on-board power $\bar{P}_{ob}$ (kW)	<b>2</b>	<b>9</b>	<b>37</b>
Additional on-board mass $\Delta m$ (kg)	<b>2</b>	<b>5</b>	<b>20</b>
Required ground area $A_g$ (m <sup>2</sup> )	<b>132</b>	<b>192</b>	<b>428</b>

**Table 20.1** Design parameters for the take-off. Bold-faced parameters are the results obtained according to the assumptions and analysis described in Sects. 20.3.1 and 20.3.2. If only one numerical value is given per line, then this value holds for all three aircraft

- The required on-board power is rather small because the aircraft does not need to be accelerated any further.
- On-board propellers and batteries are necessary in any case to power the on-board control systems. The use of slightly larger and more powerful on-board motors does not appear to be critical. Moreover, the on-board propellers can also be used to re-charge the batteries to supply energy to the control system during long periods of power generation.
- Since the whole setup can be built in a such a way that it is rotatable, the take-off is independent of the current prevalent wind direction.

These results indicate that the linear take-off approach will have only a rather small impact on the overall system design because it provides a good tradeoff between on-board and on-ground power. Other launching procedures would require extensive system modifications as we discussed in Ref. [7]. However, there we only considered a rigid aircraft with a fixed wing loading of  $w_l = 15 \text{ kg/m}^2$ . In Fig. 20.4, we show how the required peak power on the ground and on board depend on the wing loading, for two different wing sizes, namely 1.6 m and 10 m. This is important because it is not clear at this stage of AWE development what the typical wing loading will be and—if they turn out to be high ( $\sim 20 \text{ kg/m}^2$ )—what the impact will

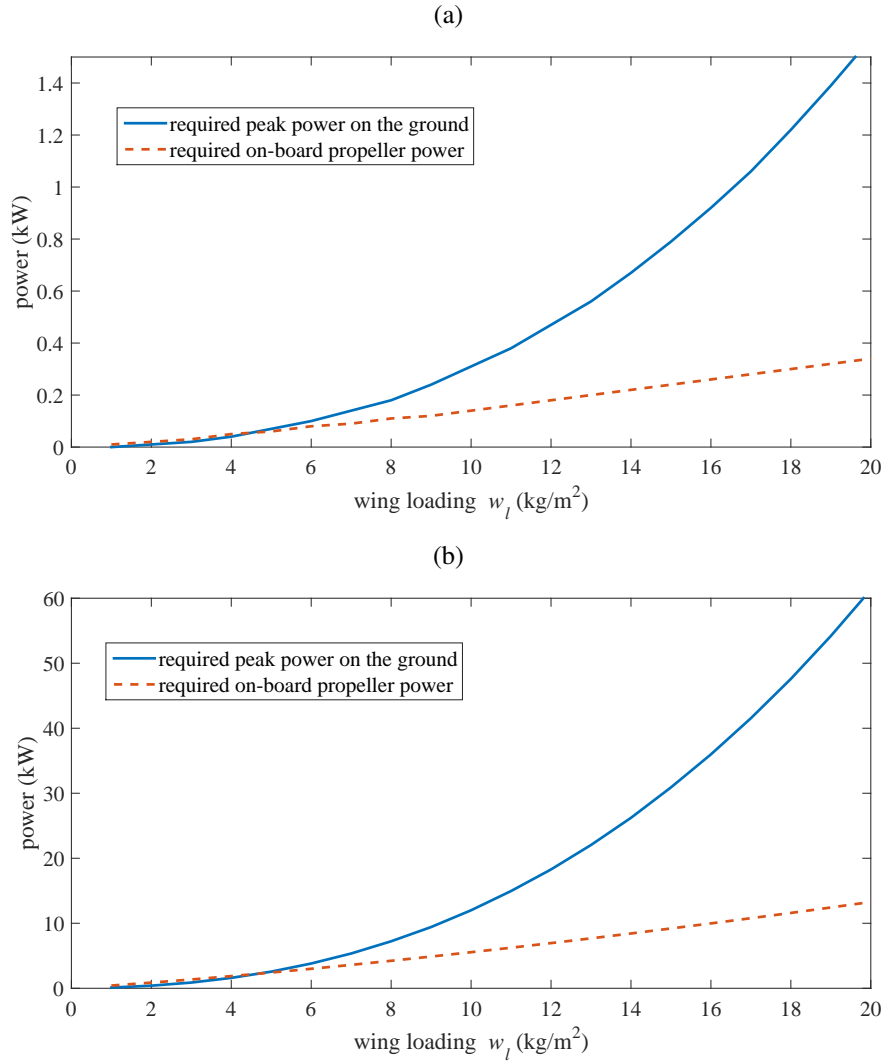


**Fig. 20.4** Required peak power for acceleration on the ground (solid line) and propeller power on board (dashed line). (a) small model aircraft like the one used in our experimental setup ( $d = 1.6$  m corresponding to 7.7 kW mechanical power with the other parameters given in Table 20.1) as a function of wing loading. (b) larger aircraft ( $d = 10$  m with 300 kW mechanical power as shown in Table 20.1) as a function of wing loading

be on the launching procedure. Apparently, the smaller the wing loading, the better for the overall system performance in terms of aircraft maneuverability, operating wind range and ultimately for the power generation capability. On the other hand,

at large power levels the structural requirements might call for stronger structures with higher wing loading.

Fig. 20.4 demonstrates that the linear launch approach in combination with small on-board propellers can also cope well with high wing loading. The required power for the on-board propellers increases linearly with the wing loading and represents only about 4% of the mechanically generated peak power for a wing loading of  $20 \text{ kg/m}^2$ , up from about 3% with  $w_l = 15 \text{ kg/m}^2$  and 2% with  $w_l = 8 \text{ kg/m}^2$ . As expected from Eq. (20.4), the power for acceleration to the take-off speed on the ground increases more than quadratically with the wing loading. However, this additional power does not affect the aircraft design. Moreover, even at high wing loadings of  $20 \text{ kg/m}^2$ , the on-ground peak power is only about 20% of the estimated generated peak mechanical power during crosswind flight. If the main winch is used for acceleration of the slide to take-off speed, high wing loadings do not present a significant disadvantage for the linear launch procedure, either.

So far, we focused our attention on the take-off phase only, and on its impact on the overall system design. In the following section, we present results concerning the full cycle of take-off, flight with low tether tension, and landing. In particular, we consider the modeling and control aspects of this strategy and study it by means of numerical simulations.

## 20.4 Modeling and Control of Linear Take-Off and Landing Maneuvers

### 20.4.1 Control Objectives and Problem Formulation

For each phase described in Sect. 20.2.2, there are specific control objectives. During the launch, the ground station shall be able to synchronously accelerate the slide and the main winch to allow the aircraft to take-off with low tether tension. During the flight phase, the on-board control unit shall follow the desired path despite the perturbation of the tether and wind. At the same time, the ground-station control system shall adapt the tether length such that the tension is low but non-zero, to have minimal impact on the aircraft's flight but at the same time avoiding tether entangling on the winch and an excessive line sag. Finally, in the landing phase, the aircraft shall land within the area covered by the rails so that it can engage with the slide again. In Ref. [14], we described a control system able to achieve the above-mentioned goals, and we showed simulation results for an aircraft with small wing loading. We recall here the main aspects of the control strategy, provide simulation results for an aircraft with larger wing loading, and compare them with the ones presented in Ref. [14].

### 20.4.2 Mathematical Model of the System

We describe the system dynamics with a hybrid model (see Fig. 20.5): a first operating mode accounts for the system's behavior from zero speed to the take-off speed, during which the aircraft and the slide can be considered as a unique rigid body; a second operating mode describes the aircraft motion after take-off, when it is separated from the slide.

We consider an inertial, right-handed reference frame  $(X, Y, Z)$  with the origin corresponding to the central point of the rails, which are assumed parallel to the ground, the  $X$ -axis aligned with them, and the  $Z$ -axis pointing downwards, see Fig. 20.1. We denote a generic vector in the three-dimensional space as  $\mathbf{v}$  and we specify the reference frame considered to compute the vector's components with a subscript notation, e.g.  $\mathbf{v}_{(XYZ)}$ . Each scalar component of the vector will be followed by its axis, i.e.  $\mathbf{v}_{(XYZ)} = [v_X, v_Y, v_Z]^T$ . For the sake of brevity, we omit the explicit dependence of the model variables on the continuous time  $t$ .

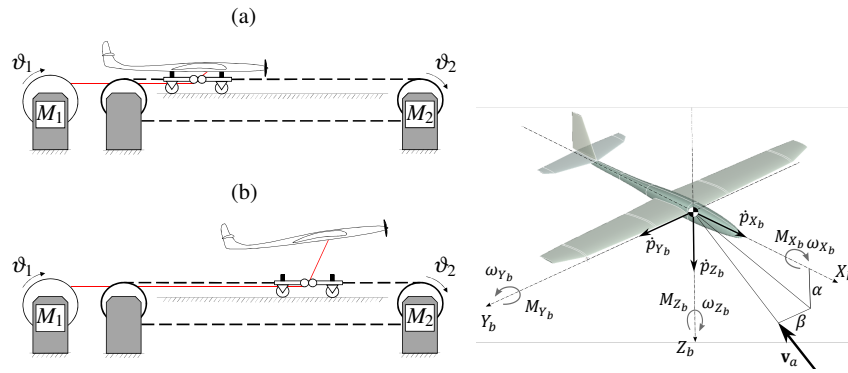


**Fig. 20.5** Sketch of the dynamical model. Left: (a) First operating mode, with the aircraft carried by the slide up to take-off speed; (b) second operating mode, with the aircraft detached from the slide. Right: Variables and parameters describing the flight expressed in the body frame of reference.  $\omega_{x_b}$  is the roll rate,  $\dot{p}_{y_b}$  is the pitch rate, and  $\omega_{z_b}$  is the yaw rate.  $\alpha$  and  $\beta$  are the velocity angles or the angle of attack and the side slip angle, respectively

In the model of the ground station, we denote the motor/generator linked to the winch with  $M_1$  and with  $M_2$  the one connected to the slide drum.  $\vartheta_1, \dot{\vartheta}_1, \vartheta_2, \dot{\vartheta}_2$  denote the angular positions and speeds of  $M_1$  and  $M_2$ , respectively, while  $u_{M_1}, u_{M_2}$  denote the torques applied by the motors. The state and input vectors of the ground-station model are then given by

$$\begin{aligned} x_{GS} &\doteq [\vartheta_1, \dot{\vartheta}_1, \vartheta_2, \dot{\vartheta}_2]^T, \\ u_{GS} &\doteq [u_{M_1}, u_{M_2}]^T. \end{aligned} \quad (20.9)$$

The dynamical model of the ground station accounts for inertia and viscous friction of the winch and of the linear motion system and for the external forces exerted by the aircraft (lift, drag and inertia) and by the tether when under tension. The switch between the first and second operating mode occurs when the lift force developed by the aircraft equals its weight, hence lifting it from the slide. From that instant on, the ground station and the aircraft are considered as separate rigid bodies. The full model equations of the ground station are omitted here for brevity; the interested reader is referred to Ref. [14] for the full details.

To model the aircraft's dynamics after detaching from the slide, we consider the body reference frame  $(X_b, Y_b, Z_b)$ , represented in Fig. 20.5, which is fixed to the plane and whose rotation relative to the inertial frame  $(X, Y, Z)$  is defined by the Euler angles  $\phi$  (roll),  $\theta$  (pitch) and  $\psi$  (yaw). Denoting with  $\omega$  the angular velocity vector of the aircraft (see Fig. 20.5), we have:

$$\begin{aligned}\dot{\phi} &= \omega_{X_b} + (\omega_{Y_b} \sin(\phi) + \omega_{Z_b} \cos(\phi)) \tan(\theta), \\ \dot{\theta} &= \omega_{Y_b} \cos(\phi) - \omega_{Z_b} \sin(\phi), \\ \dot{\psi} &= \frac{1}{\cos(\theta)} (\omega_{Y_b} \sin(\phi) + \omega_{Z_b} \cos(\phi)).\end{aligned}\quad (20.10)$$

We further denote the position of the aircraft relative to the origin of the inertial system  $(X, Y, Z)$  with  $\mathbf{p}$ . The manipulated variables available for control are denoted with  $u_a$  (ailerons),  $u_e$  (elevator),  $u_r$  (rudder),  $u_f$  (flaps), and  $u_m$  (motor thrust). We then define the state and input vectors of the aircraft model as:

$$\begin{aligned}x_g &\doteq [p_X, p_Y, p_Z, \dot{p}_{X_b}, \dot{p}_{Y_b}, \dot{p}_{Z_b}, \phi, \theta, \psi, \omega_{X_b}, \omega_{Y_b}, \omega_{Z_b}]^\top, \\ u_g &\doteq [u_a, u_e, u_r, u_f, u_m]^\top,\end{aligned}\quad (20.11)$$

as well as the full system's state and input vectors as:

$$\begin{aligned}x &\doteq \begin{bmatrix} x_{GS} \\ x_g \end{bmatrix} \in \mathbb{R}^{16}, \\ u &\doteq \begin{bmatrix} u_{GS} \\ u_g \end{bmatrix} \in \mathbb{R}^7.\end{aligned}\quad (20.12)$$

For a given wind vector  $\mathbf{v}_w$ , the apparent wind speed  $\mathbf{v}_a$  is given by:

$$\mathbf{v}_a = \mathbf{v}_w - \dot{\mathbf{p}}.\quad (20.13)$$

We denote the angle of attack with  $\alpha$  and the side slip angle of the aircraft with  $\beta$  (see Fig. 20.5). The angles  $\alpha, \beta$  and their time derivatives  $\dot{\alpha}, \dot{\beta}$  are used to compute the aerodynamic coefficients that, together with  $\|\mathbf{v}_a\|_2$  and the control inputs  $u_g$ , determine the magnitudes of the aerodynamic force  $\mathbf{F}_a$  and moment  $\mathbf{M}_a$ . The orientations of  $\mathbf{F}_a$ , and  $\mathbf{M}_a$  depend on the aircraft's attitude and on the control inputs as well as on  $\alpha$  and  $\beta$ . In addition to the aerodynamic effects, we include the thrust of the propellers,  $\mathbf{F}_T$ , the aircraft's weight  $\mathbf{F}_W$ , and the force  $\mathbf{F}_t$  and moment  $\mathbf{M}_t$  exerted by the tether. The tether force is computed by considering its elasticity, aerodynamic drag and weight, which are functions of its length. The total force and

moment applied to the aircraft are then computed as  $\mathbf{F} = \mathbf{F}_a + \mathbf{F}_W + \mathbf{F}_t + \mathbf{F}_T$  and  $\mathbf{M} = \mathbf{M}_a + \mathbf{M}_t$ , respectively. They are, in general, a function of the full system's state  $x$  and input  $u$ . We make the following main assumptions:

- The earth is assumed to be flat and serves as inertial reference.
- The aircraft is a rigid body with constant mass.
- The flight takes place at very low Mach number; thus the compression effects are neglected.
- The body axis lies in the plane of symmetry of the glider.
- The coupling between the longitudinal and the lateral motion is negligible.

Based on the above definitions and assumptions, we can write the model dynamics as a system of first-order non-linear differential equations:

$$\dot{x} = f(x, u, \mathbf{v}_w) \quad (20.14)$$

For the sake of space, we omit the full derivation of the forces and of the model equations here (see Refs. [14] and [3] for the full details).

### 20.4.3 Control Design

We propose a decoupled control approach, where the controller of the ground station (respectively of the aircraft) computes the values of  $u_{GS}$  (resp.  $u_g$ ) according to local information. Thus, there is no active communication between the aircraft and the ground station. Rather, the coordination between the two control systems is realized by exploiting the measurement of the tether tension. We further assume that the two controllers are aware of whether the aircraft is on the slide (first operating mode in Sect. 20.4.2) or not (second operating mode). This information can be easily obtained with contact or proximity sensors installed on both the ground station and the aircraft.

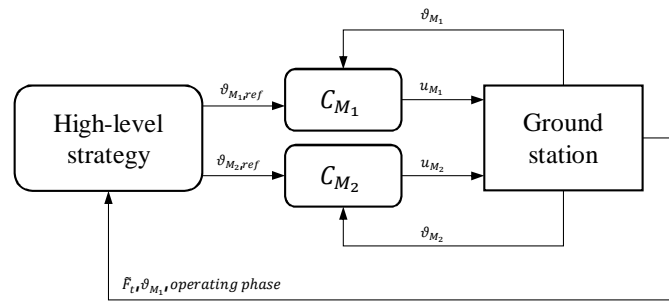


**Fig. 20.6** Controller for the ground station. The “operating phase” in the outer feedback path refers to whether the system is into the first or second operating mode; this is a Boolean type of information that can be detected by means of e.g. a proximity switch.

The controller for the ground station is hierarchical (see Fig. 20.6): two low-level position control loops track the reference angular positions for motors  $M_1$  and  $M_2$ , issued by a high-level strategy. The low-level controllers  $C_{M_1}, C_{M_2}$  are linear, designed using standard loop-shaping techniques [15] since the ground station dynamics are essentially linear as long as the tether force is kept at zero, i.e. when the tether is slightly slack. Hard limits  $\bar{u}_{M_1}, \bar{u}_{M_2}$  on the magnitude of the torques  $u_{M_1}, u_{M_2}$  that the motors can deliver are accounted for as simple saturations of the input in the control strategy.

On the other hand, the high-level controller changes on the basis of the operating mode. During the take-off, a step reference position equal to the desired take-off travel is issued to the slide controller. During the consequent motion, the slide reaches the take-off speed. At the same time, the reference position for the winch motor is latched to the slide movement. After take-off, the slide motor is stopped, while the winch motor employs a reeling strategy aimed to control the load on the tether, in order not to influence the aircraft's motion significantly while at the same time avoiding too large tether sag and entanglement. The full details of the described control strategy are reported in Ref. [14].

For the aircraft controller, we adopt a hierarchical approach, too, where a low-level Linear Quadratic Regulator (LQR) tracks a reference state for the aircraft velocity and attitude. A high-level controller is used to compute such a reference state in order to control the flight path.

The LQR is designed considering the linearization of the system's model around a steady state  $\mathbf{x}_{g,\text{trim}}$  and corresponding input  $\mathbf{u}_{g,\text{trim}}$ . In the approach used so far, the pair  $(\mathbf{x}_{g,\text{trim}}, \mathbf{u}_{g,\text{trim}})$  corresponds to a straight flight, constant altitude motion. The linearized dynamics are computed by neglecting the presence of the tether, which is then an external disturbance from the point of view of the aircraft's controller.

Regarding the high-level controller for the aircraft, we define a sequence of target way points in space, denoted as  $[p_{i,X}^w, p_{i,Y}^w, p_{i,Z}^w]^\top, i = 1, \dots, N$ , that are used to compute reference altitude and heading for the low-level LQR. The switching from one to the next way point is based on a proximity condition. The choice of the way points (number and position) is done manually in this study, in order to achieve a roughly rectangular flight pattern. Indeed, their position has to be adapted to the features of the aircraft, like aerodynamic efficiency and wing loading, and in general according to its maneuverability. For example, given the same aerodynamic coefficients and roll angle of the aircraft, the resulting turning radius will be larger with a larger wing loading. As a consequence, the position of the target points has to be adapted to reflect such a change of turning radius. One research direction to improve the approach described here is to select the way points via numerical optimization techniques.

For a given way-point, the high-level strategy issues two reference signals: one to control the altitude of the aircraft, and one to control its heading. The altitude controller computes a reference pitch rate  $\omega_{Y_b,\text{ref}}$  on the basis of the measured path angle  $\gamma$ , defined as:

$$\gamma \doteq \alpha - \theta, \quad (20.15)$$

where the angle of attack  $\alpha$  is defined as :

$$\alpha \doteq \arctan\left(\frac{\dot{p}_{Z_b}}{\dot{p}_{X_b}}\right), \quad (20.16)$$

A reference path angle  $\gamma_{\text{ref}}$  is derived from the current aircraft's altitude and that of the current target way-point:

$$\gamma_{\text{ref}} = \arctan\left(\frac{p_{i,Z}^w - p_Z}{p_{i,X}^w - p_X}\right). \quad (20.17)$$

Then, the reference pitch rate given to the LQR is computed as:

$$\omega_{\gamma_b, \text{ref}} = -k_\gamma(\gamma_{\text{ref}} - \gamma), \quad (20.18)$$

where  $k_\gamma > 0$  is a constant gain chosen by the control designer.

The second reference signal issued by the high-level controller is for the heading of the aircraft. The reference heading needed to reach the current target point is computed as

$$\psi_{\text{ref}} = \arctan\left(\frac{p_{i,Y}^w - p_Y}{p_{i,X}^w - p_X}\right) \quad (20.19)$$

where the four-quadrant arctangent is used. The LQR then tracks such a reference yaw angle. To obtain smooth transitions from one target point to the next, we filter the reference heading signal with a first order low-pass filter. Computing the yaw reference with Eq. (20.19) is sufficient to control the heading during the flight. However, this approach does not consider the alignment of the aircraft with the orientation of the ground station, which is required to land with high accuracy. Hence, in the landing phase another strategy is used within the high-level controller. In particular, assuming without loss of generality that the last target point is the origin of the inertial system, we consider the angle  $\beta_y$ , defined as (see Fig. 20.7):

$$\beta_y = \arctan\left(\frac{p_Y}{p_X}\right) = \beta_t + \psi \quad (20.20)$$

where  $\beta_t$  is the angle between the tether projected on the ground, and the inertial  $X$ -axis, as shown in Fig. 20.7. In a way similar to the altitude controller described by Eqs. (20.17) to (20.18), we set a reference yaw rate as:

$$\dot{\psi}_{\text{ref}} = k_\beta(\beta_{y, \text{ref}} - \beta_y) \quad (20.21)$$

with  $k_\beta$  being a design parameter. In order to align the aircraft with the rails, we set  $\beta_{y, \text{ref}} = 0$  throughout the landing maneuver.

We refer the reader to Ref. [14] for the stability and robustness analysis of this high-level controller, as well as for a brief stability analysis of the closed-loop dynamics when both the high-level and low-level loops are implemented. For an air-

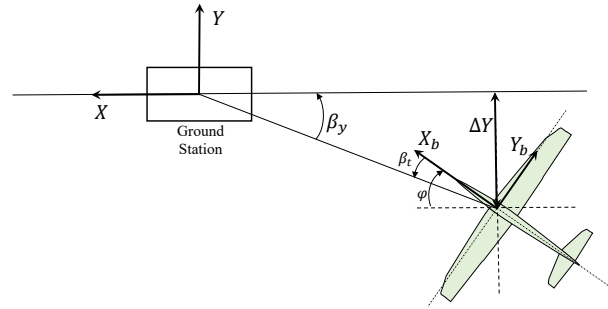


**Fig. 20.7** Lateral positioning analysis for high-level controller design

craft with a relatively small wing loading, this approach led to satisfying results. Here, we employ the same approach for an aircraft with larger wing loading. In this case, as we will further comment in Sects. 20.5 and 20.6, it turns out that the increased mass renders the control problem more difficult and can lead to stall behaviors in some circumstances, e.g. in presence of strong turbulence, and to lower landing accuracy. Hence, more sophisticated control approaches like gain scheduling for the low-level and trajectory tracking algorithm for the high level might be required. On the other hand, for moderate or no turbulences, the simple approach with a fixed LQR coupled with the high-level controllers described earlier, is able to achieve the prescribed tasks with good performance also with the larger wing loading.

## 20.5 Simulation Results

We implemented the model and the control system in Matlab/Simulink. The main parameters of the ground station and of the aircraft are described in Table 20.2. In addition, the values  $\rho = 1.2 \text{ kg/m}^3$ ,  $g = 9.81 \text{ m/s}^2$  were used for the air density and gravity acceleration.

These parameters correspond to an aircraft with the same design as the one considered in Ref. [14], but wing loadings of  $3.8 \text{ kg/m}^2$  and  $8 \text{ kg/m}^2$ . Similarly to what is discussed in Ref. [14], we computed the aerodynamic coefficients using XFRLR5 [13]. The numerical values for the lighter aircraft are reported in Ref. [14], while those for the heavier one are omitted for the sake of space.

### 20.5.1 Take-Off Phase

Examples of simulation results for the take-off phase are shown in Figs. 20.8 and 20.9, for the higher wing loading of  $8 \text{ kg/m}^2$ . In Fig. 20.8(a), it can be noted that

Ground station parameters		Aircraft and tether parameters	
Winch radius	0.1 m	Wingspan	1.68 m
Slide drum radius	0.1 m	Aspect Ratio	8.9
Winch m. of inertia	0.08 kg m <sup>2</sup>	Wing loading	{3.8, 8} kg/m <sup>2</sup>
Slide drum m. of inertia	0.01 kg m <sup>2</sup>	Mass	{1.2; 2.54} kg
Winch visc. fr. coeff.	0.04 kg m <sup>2</sup> /s	Propeller power	{320; 600} W
Slide drum visc. fr. coeff.	0.01 kg m <sup>2</sup> /s	Peak motor thrust	{8; 16.6} N
Slide mass	2 kg	Tether Young mod.	5.3 × 10 <sup>9</sup> Pa
Visc. friction coeff. of rails	0.6 kg/s	Tether breaking elong.	0.02
Peak torque $M_1$	220 N m	Tether drag coeff.	1
Peak torque $M_2$	22 N m	Tether diameter	0.002 m

**Table 20.2** Simulation parameters for aircraft with wing loadings of 3.8 kg/m<sup>2</sup> and 8 kg/m<sup>2</sup>

the total travel distance of the slide is equal to about 5 m, and that the aircraft starts the ascend after 2.9 m, i.e. when the take-off speed of 13 m/s has been reached. As shown in Fig. 20.8(b), the slide motor exploits the full rated torque to accelerate and then to brake the slide. The propeller is engaged only after take-off and, after a short transient, it settles to a steady value sufficient to achieve the desired vertical velocity, see Fig. 20.9(a). Fig. 20.9(b) presents the power consumption of the slide motor, winch motor and propellers during the take-off. The simulated peak power values are 3 kW to accelerate the slide, and 0.5 kW for the ascend phase. The former value is in line with the theoretical results of Sect. 20.3 which provide, for the same parameters, 3.1 kW for the ground acceleration. On the other hand, the on-board power predicted by the simulation is larger than the 0.1 kW given by the theoretical results, essentially due to a larger climb rate (twice the one considered

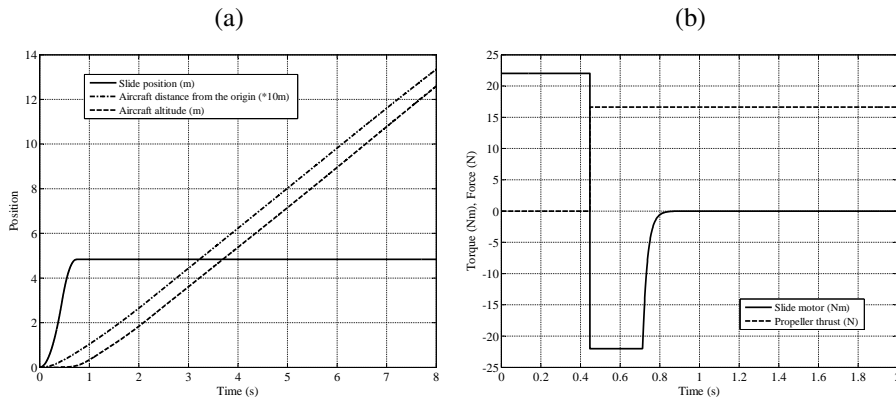


**Fig. 20.8** Simulation results for (a) courses of the aircraft height, slide position and aircraft distance from the ground station (divided by 10 for the sake of clarity) and (b) courses of the slide motor torque and of the propeller thrust. Wing loading: 8 kg/m<sup>2</sup>

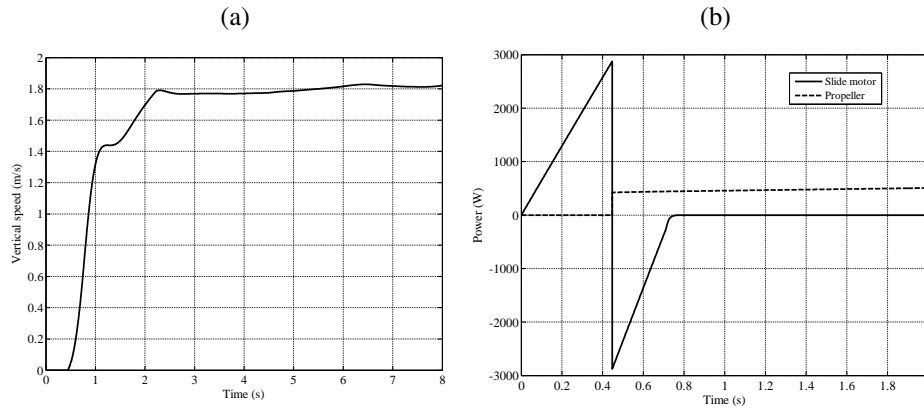


**Fig. 20.9** Simulation results for (a) course of the vertical speed of the aircraft and (b) courses of the slide motor's and propeller's power. Wing loading:  $8 \text{ kg/m}^2$

in Sect. 20.3), due to the pitch of the aircraft, which has the effect of decreasing the thrust in horizontal direction and adding a braking contribution from the lift force projected onto the  $x_g$ -axis, and due to the fact that in the simulation the plane operates at a lift coefficient of 0.6. The on-board power is anyways a reasonably small fraction (approximately 5%) of the system's power.

The results obtained with the lower wing loading, i.e.  $3.8 \text{ kg/m}^2$ , are qualitatively identical. The aircraft in this case takes off after 1.1 m at a take-off speed of about 9 m/s. The simulated peak power values are 2 kW to accelerate the slide, and 0.2 kW for the ascend phase. The same considerations as those drawn above for the higher wing loading, about the matching between the theoretical results and the simulations, hold also in this case.

### 20.5.2 Flight and Landing Phases

In Fig. 20.10(a), we present the flight patterns for an aircraft with  $3.8 \text{ kg/m}^2$  wing loading (the same as considered in Ref. [14]) and for  $8 \text{ kg/m}^2$ , with the main parameters reported in Table 20.2. As discussed in Sect. 20.4.3, a larger wing loading leads to a larger flight pattern, with longer climbing and approaching phases. The reasons for this behavior are essentially the larger velocity required by the heavier aircraft (while the climbing velocity remains the same) combined with the increased inertia, while the maximum position of the control surfaces and the maximum roll and pitch angles are roughly the same. In other words, the increased mass requires a larger fraction of the lift force to be exploited to keep the aircraft airborne, leaving a smaller lift contribution available for maneuvering, hence increasing the minimum turning radius. Another approach to reduce the turning radius could be to exploit the tether tension in order to enforce geometrically the pattern curvature, eventually

by reeling-in during the turn. Fig. 20.10(b) shows the tether load during the whole cycle. A low tension is kept throughout the flight, notwithstanding the pronounced changes in tether length, also shown in Fig. 20.10(b), which matches closely the distance between the aircraft and the origin. This result indicates that indeed it should be possible to avoid continuous communication between the ground station and the aircraft and still obtain satisfactory results. Our recent experimental results further confirm this aspect [5]. If available, communication could be then added to further improve the performance, e.g. by injecting additional apparent wind speed by reeling-in in case of close-to-stall situations

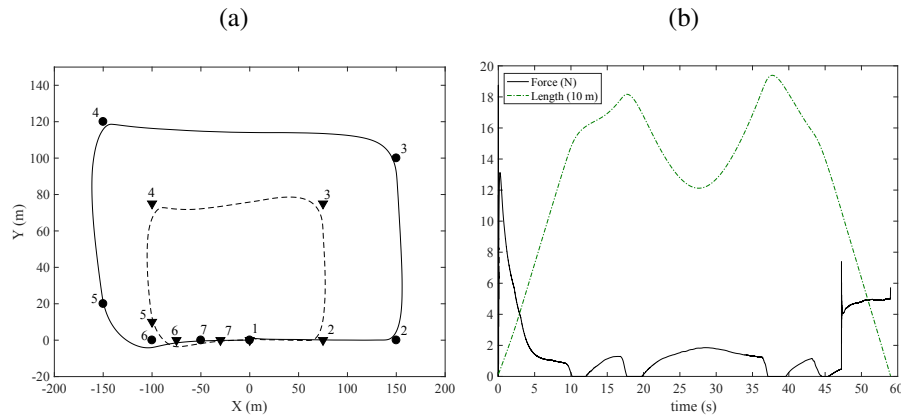


**Fig. 20.10** Simulation results: (a) A three-dimensional illustration of the flight path with reference points for the aircraft with  $3.8 \text{ kg/m}^2$  wing loading (dashed) and with  $8 \text{ kg/m}^2$  wing loading and (b) tether tension (solid) and length (dashed) for the aircraft with  $8 \text{ kg/m}^2$  wing loading

Since the high-level controller is based on way points instead of a trajectory tracking approach, and since such way points are different between the two considered aircraft due to their different wing loading, evaluating the tracking performance of the controller during the low-tension flight is of little interest. Instead, comparing the landing positioning performance between the two aircraft and as a function of the wind conditions is of high interest for the sake of this study. To this end, a comparison of the positioning precision achieved by the two aircraft in the landing phase is shown in Fig. 20.11. We consider increasing nominal wind speed (aligned with the rails such that take-off and landing are performed with the aircraft facing the incoming wind) and random wind disturbances with an amplitude equal to 30% of the nominal speed in all three directions. We compute 50 simulated flights for each nominal wind speed and each aircraft. The obtained positioning precisions are shown, in terms of average  $X$  and  $Y$  positions,  $\bar{X}$  and  $\bar{Y}$ , and standard deviations  $\sigma_X$  and  $\sigma_Y$ , in Table 20.3, together with the statistics of the horizontal landing speed (average  $\bar{V}$  and standard deviation  $\sigma_V$ ) and of the unsuccessful landings.

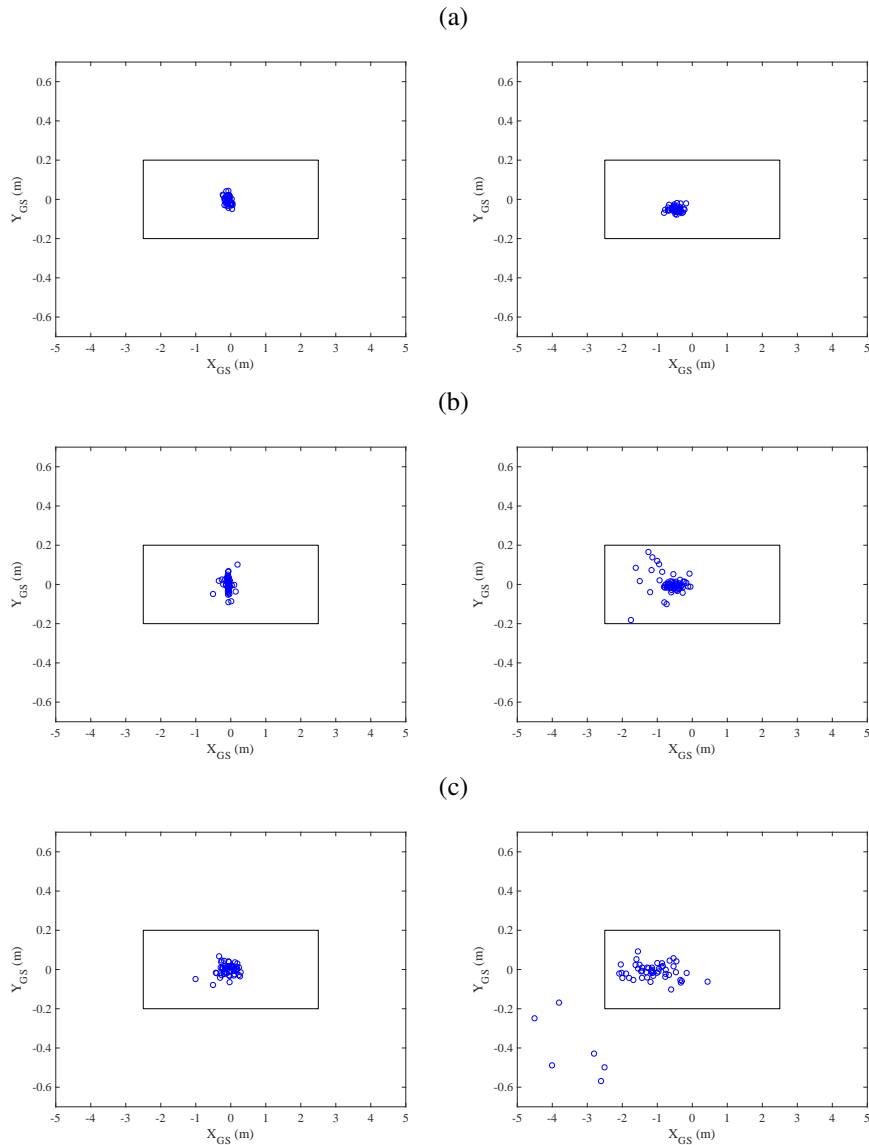


**Fig. 20.11** Simulation results. Touch-down position for the aircraft with  $3.8\text{ kg/m}^2$  wing loading (left plots) and for  $8\text{ kg/m}^2$  wing loading (right plots) with nominal wind of (a) 2 m/s, (b) 4 m/s and (c) 6 m/s and uniformly distributed 3D wind disturbances in the range of  $\pm 30\%$  of the nominal wind. The rectangle in the plots correspond to the dimensions of the rails (note the different scales of the two axes)

Figures 20.11(a) to (c) show the touch-down points on the ground station with the origin being in the middle of the rails which cover an area of  $0.4\text{ m} \times 5\text{ m}$ . With

Nom. wind	$\bar{X}$ (m)	$\sigma_X$ (m)	$\bar{Y}$ (m)	$\sigma_Y$ (m)	$\bar{V}$ (m/s)	$\sigma_V$ (m/s)	Failures (%)
Wing loading: 3.8 kg/m <sup>2</sup>							
0 m/s	0.18	0.03	-0.002	0.03	16.2	2.3	0
2 m/s	-0.07	0.07	-0.004	0.013	15.0	2.2	0
4 m/s	-0.06	0.1	0.005	0.026	12.9	1.9	0
6 m/s	-0.02	0.16	-0.003	0.034	10.6	1.7	0
Wing loading: 8 kg/m <sup>2</sup>							
0 m/s	-0.46	0.14	-0.05	0.035	17.1	2.5	0
2 m/s	-0.45	0.17	-0.007	0.017	15.0	2.18	0
4 m/s	-0.54	0.54	0.015	0.046	12.5	2.14	4
6 m/s	-1.01	1.65	-0.11	0.31	10.6	2.4	4

**Table 20.3** Landing precision and velocities for different wind conditions. For each nominal wind speed, wind gusts with a magnitude of  $\pm 30\%$  of the nominal wind are considered. For the case of zero nominal wind speed, wind gusts of  $\pm 1$  m/s are considered

increasing nominal wind speed, the average touch-down point is pushed backwards and the lateral positioning accuracy improves. This is due to the fact that a higher front wind reduces the aircraft's speed relative to ground, hence giving more time to align with the rails. These effects are expected and indicate a good overall performance of the control system.

For the lighter aircraft, touch-down is always within the area spanned by the rails. For the heavier aircraft, the situation is more critical. In fact, with the strongest nominal wind speed (6 m/s), in 4% of the cases the aircraft stalls during the flight. In 14% of the cases, the controller is not able to land the aircraft on the rails, finally the average accuracy of the successful landings is worse than that obtained with the lighter aircraft. The main reasons for this outcome are similar to what is discussed above, i.e. the larger mass reduces maneuverability and makes it more difficult to counteract the wind disturbances. Moreover, the wider flight trajectory implies a longer tether, with consequently larger weight and drag with respect to the case of the lighter aircraft. Using a more advanced control approach (e.g. gain scheduling) might help improving robustness, as well as having more powerful on-board propellers, a more efficient wing design and larger actuation limits of the control surfaces, or even additional control surfaces.

## 20.6 Conclusions and Future Developments

We presented an overview of recent results pertaining to the take-off and landing phases of AWE systems based on a rigid aircraft and pumping-power conversion. A theoretical analysis derives the main links among the ground and on-board power, the on-board mass, and the land occupation required to carry out the take-off. A

simulation study further shows the system behavior in a full cycle consisting of take-off, low-tension flight and landing again on the rails used for the initial start-up. A decentralized control approach to carry out the cycle is described as well.

Regarding the take-off phase, the results indicate that the additional ground and on-board equipment constitutes a rather small cost fraction of the total system costs, even with large wing loading. At the same time, the required land occupation is reasonably small.

On the other hand, when it comes to the low-tension flight and landing phases, the mass has an important effect on stability and landing accuracy, so that a trade-off between maneuverability, wing loading and on-board power has to be achieved. Better control strategies and ad-hoc wing design and actuators can mitigate the issue, and this will be subject of future research. For example, one could schedule the controller according to the incoming airspeed, employ feed-forward contributions to improve the control response time, or develop additional control strategies which, for example, could monitor the behavior during landing and eventually decide to take-off again before touch-down and then attempt another landing.

In summary, the present study shows that the wing loading is a crucial parameter in the system design not only for power generation, where it affects the cut-in and cut-out wind speeds, the flight trajectory, and ultimately the overall capacity factor, but also for the landing phase. Which condition is the most critical one and hence provides the main design criteria for the whole system is also a subject of future studies. It is well true that similar results, concerning the effects of wing loading on take-off, flight and landing for aircraft, are largely available in the literature of flight dynamics, however without considering the tether. The added value of our study in this respect is to study these aspects also when the tether is present. Another finding of our research is that with a proper force measurement and a large enough torque of the winch motor, the coordination between the winch and the aircraft can be carried out without active communication among the two, since the winch can react fast enough to avoid stalling the plane. This behavior can be further improved by using a damping system on the ground, e.g. by means of a mass-spring-damper system, and by using the measured state of such a system to improve the winch control strategy.

Recent experimental tests carried out at ABB Switzerland, Corporate Research, demonstrated the feasibility of autonomous launch and low-tension flight of a small rigid aircraft. The employed approach and results are presented in Refs. [4, 5].

## References

1. Ampyx Power B.V. <http://www.ampyxpower.com/>. Accessed 6 Feb 2017
2. Bontekoe, E.: How to Launch and Retrieve a Tethered Aircraft. M.Sc.Thesis, Delft University of Technology, 2010. <http://resolver.tudelft.nl/uuid:0f79480b-e447-4828-b239-9ec6931bc01f>
3. Etkin, B.: Dynamics of Atmospheric Flight. Dover Publication, New York, NY (1972)
4. Fagiano, L., Nguyen-Van, E., Rager, F., Schnez, S., Ohler, C.: A Small-Scale Prototype to Study the Take-Off of Tethered Rigid Aircrafts for Airborne Wind Energy. IEEE/ASME Transactions on Mechatronics **22**(4), 1869–1880 (2017). doi: [10.1109/TMECH.2017.2698405](https://doi.org/10.1109/TMECH.2017.2698405)

5. Fagiano, L., Nguyen-Van, E., Rager, F., Schnez, S., Ohler, C.: Autonomous Take-Off and Flight of a Tethered Aircraft for Airborne Wind Energy. *IEEE Transactions on Control Systems Technology* **26**(1), 151–166 (2018). doi: [10.1109/TCST.2017.2661825](https://doi.org/10.1109/TCST.2017.2661825)
6. Fagiano, L., Milanese, M.: Airborne Wind Energy: an overview. In: *Proceedings of the 2012 American Control Conference*, pp. 3132–3143, Montréal, QC, Canada, 27–29 June 2012. doi: [10.1109/ACC.2012.6314801](https://doi.org/10.1109/ACC.2012.6314801)
7. Fagiano, L., Schnez, S.: On the Take-off of Airborne Wind Energy Systems Based on Rigid Wings. *Renewable Energy* **107**, 473–488 (2017). doi: [10.1016/j.renene.2017.02.023](https://doi.org/10.1016/j.renene.2017.02.023)
8. Fagiano, L., Schnez, S.: The Take-Off of an Airborne Wind Energy System Based on Rigid Wings. In: Schmehl, R. (ed.). *Book of Abstracts of the International Airborne Wind Energy Conference 2015*, pp. 94–95, Delft, The Netherlands, 15–16 June 2015. doi: [10.4233/uuid:7df59b79-2c6b-4e30-bd58-8454f493bb09](https://doi.org/10.4233/uuid:7df59b79-2c6b-4e30-bd58-8454f493bb09). Presentation video recording available from: <https://collegerama.tudelft.nl/Mediasite/Play/2ebb3eb4871a49b7ad70560644cb3e2c1d>
9. Fritz, F.: Application of an Automated Kite System for Ship Propulsion and Power Generation. In: Ahrens, U., Diehl, M., Schmehl, R. (eds.) *Airborne Wind Energy, Green Energy and Technology*, Chap. 20, pp. 359–372. Springer, Berlin Heidelberg (2013). doi: [10.1007/978-3-642-39965-7\\_20](https://doi.org/10.1007/978-3-642-39965-7_20)
10. Gros, S., Zanon, M., Diehl, M.: A relaxation strategy for the optimization of Airborne Wind Energy systems. In: *Proceedings of the 2013 European Control Conference (ECC)*, pp. 1011–1016, Zurich, Switzerland, 17–19 July 2013
11. Kruijff, M., Ruitkamp, R.: Status and Development Plan of the PowerPlane of Ampyx Power. In: Schmehl, R. (ed.). *Book of Abstracts of the International Airborne Wind Energy Conference 2015*, pp. 18–21, Delft, The Netherlands, 15–16 June 2015. doi: [10.4233/uuid:7df59b79-2c6b-4e30-bd58-8454f493bb09](https://doi.org/10.4233/uuid:7df59b79-2c6b-4e30-bd58-8454f493bb09). Presentation video recording available from: <https://collegerama.tudelft.nl/Mediasite/Play/2e1f967767d541b1b1f2c912e8eff7df1d>
12. Loyd, M. L.: Crosswind kite power. *Journal of Energy* **4**(3), 106–111 (1980). doi: [10.2514/3.48021](https://doi.org/10.2514/3.48021)
13. Meschia, F.: Model analysis with XFLR5. *Radio Controlled Soaring Digest* **25**(2), 27–51 (2008). <http://www.rcsoaringdigest.com/pdfs/RCSD-2008/RCSD-2008-02.pdf>
14. Nguyen Van, E., Fagiano, L., Schnez, S.: Autonomous take-off and landing of a tethered aircraft: a simulation study. In: *Proceedings of the American Control Conference*, pp. 4077–4082, Boston, MA, USA, 6–8 July 2016. doi: [10.1109/ACC.2016.7525562](https://doi.org/10.1109/ACC.2016.7525562)
15. Skogestad, S., Postlethwaite, I.: *Multivariable Feedback Control*. 2nd ed. Wiley, New York (2005)
16. Vander Lind, D.: Analysis and Flight Test Validation of High Performance Airborne Wind Turbines. In: Ahrens, U., Diehl, M., Schmehl, R. (eds.) *Airborne Wind Energy, Green Energy and Technology*, Chap. 28, pp. 473–490. Springer, Berlin Heidelberg (2013). doi: [10.1007/978-3-642-39965-7\\_28](https://doi.org/10.1007/978-3-642-39965-7_28)
17. Vermillion, C., Glass, B., Rein, A.: Lighter-Than-Air Wind Energy Systems. In: Ahrens, U., Diehl, M., Schmehl, R. (eds.) *Airborne Wind Energy, Green Energy and Technology*, Chap. 30, pp. 501–514. Springer, Berlin Heidelberg (2013). doi: [10.1007/978-3-642-39965-7\\_30](https://doi.org/10.1007/978-3-642-39965-7_30)